Metabolic Engineering 32 (2015) 207–219

Contents lists available at ScienceDirect

Metabolic Engineering

journal homepage: www.elsevier.com/locate/ymben

Original Research Article

Elucidating central metabolic redox obstacles hindering ethanol production in *Clostridium thermocellum*

R. Adam Thompson [a,b], Donovan S. Layton [b,c], Adam M. Guss [a,b,d], Daniel G. Olson [b,e], Lee R. Lynd [b,e], Cong T. Trinh [a,b,c,*]

[a] Bredesen Center for Interdisciplinary Research and Graduate Education, The University of Tennessee, Knoxville and Oak Ridge National Laboratory, Oak Ridge, TN, USA
[b] BioEnergy Science Center, Oak Ridge National Laboratory, Oak Ridge, TN, USA
[c] Department of Chemical and Biomolecular Engineering, The University of Tennessee, Knoxville, TN, USA
[d] Biosciecnes Division, Oak Ridge National Laboratory, Oak Ridge, TN, USA
[e] Thayer School of Engineering, Dartmouth College, Hanover, NH, USA

ARTICLE INFO

Article history:
Received 21 May 2015
Received in revised form
8 October 2015
Accepted 12 October 2015
Available online 21 October 2015

Keywords:
Clostridium thermocellum
Redox metabolism
Energy metabolism
Elementary mode analysis
Minimal metabolic functionality
Ethanol

ABSTRACT

Clostridium thermocellum is an anaerobic, Gram-positive, thermophilic bacterium that has generated great interest due to its ability to ferment lignocellulosic biomass to ethanol. However, ethanol production is low due to the complex and poorly understood branched metabolism of *C. thermocellum*, and in some cases overflow metabolism as well. In this work, we developed a predictive stoichiometric metabolic model for *C. thermocellum* which incorporates the current state of understanding, with particular attention to cofactor specificity in the atypical glycolytic enzymes and the complex energy, redox, and fermentative pathways with the goal of aiding metabolic engineering efforts. We validated the model's capability to encompass experimentally observed phenotypes for the parent strain and derived mutants designed for significant perturbation of redox and energy pathways. Metabolic flux distributions revealed significant alterations in key metabolic branch points (e.g., phosphoenol pyruvate, pyruvate, acetyl-CoA, and cofactor nodes) in engineered strains for channeling electron and carbon fluxes for enhanced ethanol synthesis, with the best performing strain doubling ethanol yield and titer compared to the parent strain. *In silico* predictions of a redox-imbalanced genotype incapable of growth were confirmed *in vivo*, and a mutant strain was used as a platform to probe redox bottlenecks in the central metabolism that hinder efficient ethanol production. The results highlight the robustness of the redox metabolism of *C. thermocellum* and the necessity of streamlined electron flux from reduced ferredoxin to NAD(P)H for high ethanol production. The model was further used to design a metabolic engineering strategy to phenotypically constrain *C. thermocellum* to achieve high ethanol yields while requiring minimal genetic manipulations. The model can be applied to design *C. thermocellum* as a platform microbe for consolidated bioprocessing to produce ethanol and other reduced metabolites.

© 2015 International Metabolic Engineering Society. Published by Elsevier Inc.

1. Introduction

Sustainable energy production is a defining challenge for modern society, and achieving this goal will depend on the ability to produce fuels and chemicals from renewable sources. Consolidated bioprocessing (CBP) (Demain, 2009, Guss et al., 2012) has the appeal of combining the steps of hydrolytic enzyme production, feedstock solubilization, and fermentation of multiple sugars into a single step (van Zyl et al., 2007), with the goal of maximizing cost-efficiency of lignocellulose conversion (Lynd et al., 2008).

C. thermocellum is an anaerobic, thermophilic, gram-positive bacterium which has been considered for CBP due to its strong capability to ferment lignocellulosic feedstocks while producing ethanol and hydrogen (Lynd et al., 2005; Ragauskas et al., 2014). However, wild-type *C. thermocellum* produces a wide range of fermentative products (e.g. acetate, formate, lactate) as well as amino acids, which limits the yield of ethanol (Ellis et al., 2012). Also, the wild-type cannot grow at the high concentrations of ethanol that are industrially necessary without extensive directed evolution (Herrero and Gomez, 1980; Brown et al., 2011; Shao et al., 2011). Progress in engineering *C. thermocellum* for increased ethanol production has been made in several ways: isolating a

* Corresponding author at: Department of Chemical and Biomolecular Engineering, The University of Tennessee, Knoxville, TN, USA.
E-mail address: ctrinh@utk.edu (C.T. Trinh).

http://dx.doi.org/10.1016/j.ymben.2015.10.004
1096-7176/© 2015 International Metabolic Engineering Society. Published by Elsevier Inc.

high ethanol-tolerant mutant via adaptive evolution (Williams et al., 2007), elimination of competing carbon fermentative pathways (e.g., acetate (Tripathi et al., 2010), lactate (Biswas et al., 2014), and both acetate and lactate (van der Veen et al., 2013)), expressing an exogenous pyruvate kinase from *Thermoanaerbacter saccharolyticum* and deleting malic enzyme (Deng et al., 2013), as well as eliminating a major competitor for electrons, H_2 production (Biswas et al., 2015). None of these strategies, however, has been successful in reaching the goal of at least 90% conversion of fermentable sugars to ethanol as seen in non-cellulolytic mesophilic organisms such as *Saccharomyces cerevisiae* (Kuyper et al., 2005) and *Escherichia coli* (Yomano et al., 1998; Trinh et al., 2008).

An important obstacle to metabolic engineering of *C. thermocellum* for enhanced biofuel production is an incomplete knowledge of its metabolism. Recent studies suggest that *C. thermocellum* possesses an atypical central metabolism. For instance, the glycolysis does not have an annotated pyruvate kinase (Deng et al., 2013). Fructose-6-phosphate kinase uses pyrophosphate (PPi) instead of ATP, and GTP can substitute for ATP in several reactions which might have important implications for metabolism (Zhou et al., 2013). The pentose phosphate pathway lacks several enzymes in the oxidative branch which implies the need for alternative pathways for NADPH synthesis (Rydzak et al., 2012). The Krebs cycle is also incomplete with the lack of succinate dehydrogenase (Roberts et al., 2010). In addition, *C. thermocellum* has many transhydrogenase reactions involving ferredoxins and both NADH and NADPH.

In this work, we consolidated the current understanding of *C. thermocellum* metabolism into a predictive metabolic network model used for metabolic flux quantification and rational strain design. We characterized engineered *C. thermocellum* strains designed and constructed with significant perturbations of energy and redox pathways to validate the model. Redox perturbation involved partial and full disruption of H_2 production while energy perturbation disrupted acetate production. Their unique phenotypes were analyzed by quantitative metabolic flux distributions. Next, we used the model to elucidate the key bottleneck in the redox metabolism of *C. thermocellum* hindering high-yield ethanol production. Finally, the validated model was used as an input for elementary mode analysis (Trinh et al., 2009) to design an optimal genotype for efficient ethanol production in *C. thermocellum*.

2. Materials and methods

2.1. Strains and plasmids

C. thermocellum strains employed in this study (Table 1) were derived from the genetically tractable strain DSM 1313 with a Δ*hpt* background, allowing for a two-stage selection counter-selection method using 8-azahypoxanthine (Argyros et al., 2011). *C. thermocellum* Δ*hydG* and Δ*hydG* Δ*ech* strains were previously described (Biswas et al., 2015). The mutant Δ*hydG* Δ*pta-ack* was constructed from the Δ*hydG* strain using the plasmid pAMG498, similar to previous reports (Argyros et al., 2011; van der Veen et al., 2013), but also deleting acetate kinase. Gene loci of *hpt*, *hydG*, *ech*, and *pta-ack* are Clo1313_2927, Clo1313_1571, Clo1313_0564-0575, and Clo1313_1185-1186, respectively. To eliminate pyruvate-formate lyase (PFL) activity and create an effective Δ*pfl* strain, the parent strain or Δ*hydG* Δ*ech* strain was cultured with 6 mM sodium hypophosphite (HPP), an analog of formate and known PFL inhibitor (Unkrig et al., 1989; Rydzak et al., 2014).

Table 1
List of strains and plasmids used in this study. Abbreviations: V, *in vivo*; S, *in silico*; and HPP, sodium hypophosphite.

Strain name	Genotype/ description	Characterization method	Source
C. thermocellum DSM 1313	Wildtype		Leibniz-Institut DSMZ
M1354	DSM1313 Δ*hpt* (Parent strain)	V,S	(Argyros et al., 2011)
Δ*hydG*	M1354 Δ*hydG adhE*(D*494*G)*	V,S	(Biswas et al., 2015)
Δ*hydG* Δ*ech*	M1354 Δ*hydG* Δ*hypABFCDE-echABCDEF adhE*(D*494*G)*	V,S	(Biswas et al., 2015)
Δ*hydG* Δ*pta-ack*	M1354 Δ*hydG* Δ*pta-ack adhE* (D*494*G)*	V,S	This study
Δ*hydG* Δ*ech* Δ*pfl*	M1354 Δ*hydG* Δ*hypABFCDE-echABCDEF adhE*(D*494*G)* + HPP	V,S	This study

2.2. Growth conditions

C. thermocellum strains were cultured in a defined MTC medium containing (per liter): 5 g cellobiose, 2 g urea, 1.5 g ammonium chloride, 2 g sodium citrate tribasic dihydrate, 1.5 g citric acid monohydrate, 1 g sodium sulfate, 1 g potassium phosphate monobasic, 2.5 g sodium bicarbonate, 1 g magnesium chloride hexahydrate, 0.2 g calcium chloride dihydrate, 0.1 g iron (II) chloride tetrahydrate, 1 g L-cysteine HCl, 20 mg pyridoxamine dihydrochloride, 4 mg p-aminobenzoic acid, 2 mg biotin, 2 mg vitamin B12, 1.25 mg manganese chloride tetrahydrate, 0.5 mg cobalt chloride hexahydrate, 0.125 mg zinc chloride, 0.125 mg copper chloride dihydrate, 0.125 mg boric acid, 0.125 mg sodium molybdate dihydrate, and 0.125 mg nickel chloride hexahydrate (Ozkan et al., 2001; Zhang and Lynd, 2003; Kridelbaugh et al., 2013). Balch tube studies were conducted with 10 mL MTC plus the appropriate additional chemicals where noted. For bottle studies and inoculum preparation, 120 mL serum bottles were prepared with 90 mL MTC. Balch tube and serum bottle cultures also contained 5 g L^{-1} MOPS for buffering, starting at a pH adjusted to 7.4 with 5 M KOH. Bottles and tubes were sealed with butyl rubber stoppers and aluminum seals, while the head space contained a N_2:CO_2 (90:10) mixture. Cells were maintained at −80 °C prior to initial inoculation. Inocula were incubated in water baths set at 55 °C.

Bioreactor studies were conducted with a Biostat B+ (Sartorius Stedim US, Bohemia, NY) dual 1.5 L fermentation system at a working volume of 1 L MTC media with MOPS omitted. Prior to inoculation, freshly prepared media were autoclaved and sparged overnight with a N_2:CO_2 (90:10) gas mixture at 500 mL/min at 55 °C. Inoculation used ~10% v/v mid-log phase cell culture to give a starting optical density of 0.05 in bioreactors. At inoculation, the gas flow was slowed to 150 mL/min, and the gas input was altered to flush the headspace only. The culture was maintained at pH 7.0 with 5 M KOH and 40% H_3PO_4, an agitation rate of 200 rpm, and a temperature of 55 °C. Batch bioreactor studies were performed at least in duplicate. For each run, triplicate samples were collected and analyzed at each time point. The fluxes, titers, and yields were reported as mean ± standard deviation for all samples.

Optical density (OD) was measured via a spectrophotometer at 600 nm (Spectronic 200+, Thermo Fisher Scientific, Inc.) To establish a calibration curve between dry cell weight (DCW) and OD (i.e., 0.502 g DCW = 1 OD_{600}, $R^2 > 0.95$) 80 mL culture samples at known optical densities were centrifuged and washed twice with 0.9% (w/v) NaCl in water. Washed cell pellets were then oven dried at 70 °C for at least three days, until DCW was stable. The calibration curve was constructed from at least two different cell

samples for several different OD measurements. An elemental DCW composition of $C_4H_7O_2N$ (101 g/mol) was used to calculate DCW in moles (Rydzak et al., 2009).

2.3. Analytical methods

For all studies, substrate and product concentrations were quantified by using a Shimadzu high pressure liquid chromatography (HPLC) system. One mL aliquots of culture were centrifuged, then the supernatants filtered at 0.2 micron and run on an Aminex 87H (Biorad Inc., Hercules, CA) column using a refractive index detector (RID) to monitor glucose consumption with lactate, formate, acetate, pyruvate, and ethanol production by an established method (Trinh et al., 2008).

Gas chromatography coupled with mass spectrometry (GC/MS) was also used to quantify extracellular amino acids. At each measured time point during fermentation, 100 μL aliquots of cell culture were centrifuged at 25,200 rcf for 5 minutes and cell supernatants collected for secreted amino acid analysis. Amino acids were then derivatized using the EZ-faast™ Free/Physiological Amino Acid GC/MS kit (Model # KG0-7166, Phenomenex Inc., Torrence, CA, USA). The manufacturer's protocols for derivatization and GC/MS separation/analysis were followed, and the concentrations of secreted amino acids were calculated from calibration curves with standard mixtures provided by the kit as well as control mixtures made in-house.

2.4. Real-time gas measurement from bioreactor runs

H_2 monitoring was accomplished in real-time using a universal gas analyzer (UGA-300) equipped with an RGA probe (SRS Inc., Sunnyvale, CA, USA) connected to the gas effluent stream from the bioreactor system. The UGA-300 was equipped with a multiple inlet valve for the concurrent sampling from both bioreactor vessels. Exhaust gases (mainly N_2, H_2, and CO_2) from the bioreactor vessels were monitored by in-line mass flow meters (Cole Palmer, Vernon Hills, IL) calibrated for a N_2:CO_2 mixture to allow for accurate calculation of H_2 concentration. The pressure within the reactor was maintained at 1.5 atm with a ball-type pressure relief valve in series with the effluent stream, downstream of the mass flow meter and before reaching the UGA-300. Accumulative H_2 (n_{H_2} in mole) were determined by the following formula:

$$n_{H_2} = \int_0^t \frac{P \cdot v}{R \cdot T} \cdot X_{H_2} \cdot \mathrm{dt} \tag{1}$$

where t (hr) is the fermentation time, P (Pa) is the pressure of the reactor, v (m^3/hr) is the volumetric flow rate, R (J/mol/K) is the ideal gas constant, T (K) is temperature, and X_{H_2} is the molar fraction of H_2.

Carbon dioxide production was not measured directly due to the presence of CO_2 in the influent gas causing fluctuations in the CO_2 signal from the UGA-300. The fluctuations were sufficient to disrupt an accurate measurement of CO_2 concentration. In this study, the CO_2 production was estimated from the concentrations of ethanol, acetate, formate, and cell mass at specific time points during the fermentation by the formula:

$$[CO_2] \triangleq [\text{ethanol}] + [\text{acetate}] + 0.5461\,[\text{cellmass}] - [\text{formate}] \tag{2}$$

where square brackets represent concentrations of respective species. The scalar operator for cell mass represents the sum of the requirement of acetyl-CoA and α-ketoglutarate minus the requirement of oxaloacetate for cell mass synthesis (Deng et al., 2013) (Supplementary Table S1). It should be noted that DCW and cell mass are used interchangeably throughout the manuscript.

2.5. Determination of experimental fluxes

Concentration profiles of 11 potentially prominent components of the fermentation broth (i.e., cellobiose, glucose, succinate, lactate, pyruvate, acetate, ethanol, formate, CO_2, H_2, and cell mass) were determined at each time point. Concentrations of all 20 major amino acids were measured during exponential growth and at the final time point, and the prominent species were included in flux analysis and carbon balance. Their fluxes were determined as follows:

$$r_P = \mu \cdot Y_{P/X} = \mu \cdot \frac{\mathrm{d[P]/dt}}{\mathrm{d[X]/dt}} \tag{3}$$

where r_P (mmol/ g DCW/hr) is the specific consumption/production rate (or flux) of metabolite P; μ (hr^{-1}) is the specific growth rate; $Y_{X/P}$ is the yield of metabolite P per unit cell mass X; and [P] (mmol/L) and [X] (mmol/L) are the concentrations of metabolites P and X, respectively.

2.6. Construction of C. thermocellum model for metabolic pathway analysis

A metabolic network was constructed for *C. thermocellum* which utilized cellobiose, a representative substrate for cellulosic biomass, as the sole carbon source (Fig. 1, Supplementary Table S1). The network reconstruction was based on the publically available curation of the DSM 1313 genome sequence (Feinberg et al., 2011) as well as an extensive literature review. The model accounts for the strict anaerobic metabolism of *C. thermocellum* which does not use the canonical forms of Embden-Meyerhof glycolysis (Zhou et al., 2013), the pentose phosphate pathway (Rydzak et al., 2012), or the Krebs (tricarboxylic acid, TCA) cycle (Roberts et al., 2010). In addition, the export of major fermentative products (i.e., ethanol, acetate, lactate, formate, and H_2), CO_2, valine, and DCW were included in the model. The biomass term was constructed following a composition described previously (Gowen and Fong, 2010; Roberts et al., 2010), adjusting amino acid and G+C content for *C. thermocellum* DSM 1313. All cellular components are derived from 12 precursor metabolites (Neidhardt et al., 1990). Total ATP requirement for DCW synthesis (i.e., $Y_{ATP}^{max} = 42.7$ mmol ATP/g DCW) was estimated following the well-established protocol (Stouthamer, 1973). The maintenance energy requirement was modeled as a separate stoichiometric reaction.

Briefly, our model proceeds from cellobiose uptake via an ATP-binding cassette transporter and cleavage via cellobiose phosphorylase (Ng and Zeikus, 1982; Nochur et al., 1992). Glucose subunits are then processed through glycolysis until the phosphoenolpyruvate (PEP) step, where PEP can be converted to pyruvate through two branches: (i) inter-conversion to oxaloacetate and malate through the "malate shunt", effectively transferring electrons from NADH to NADPH in a transhydrogenase type of mechanism, (ii) decarboxylation of oxaloacetate to pyruvate via oxaloacetate decarboxylase (ODC), and (iii) direct conversion to pyruvate coupled with ATP production via pyruvate phosphate dikinase (PPDK). Enzymes in these pathways are transcribed (Riederer et al., 2011) and translated (Rydzak et al., 2012) according to recent reports, despite PPDK enzymatic activity not being confirmed in cell-free extracts (Zhou et al., 2013).

Redox metabolism of *C. thermocellum* is complex, with multiple potential pathways available for redox cofactor recycling (Carere et al., 2012). Our model incorporated detailed electron shuttling reactions, consistent with the most recent understanding (Rydzak et al., 2014). Most prominently represented in *C. thermocellum* is a complicated system which shuttles electrons between reduced ferredoxin, NADH, and NADPH using several different enzyme complexes including reduced ferredoxin:NAD(P) oxidoreductases

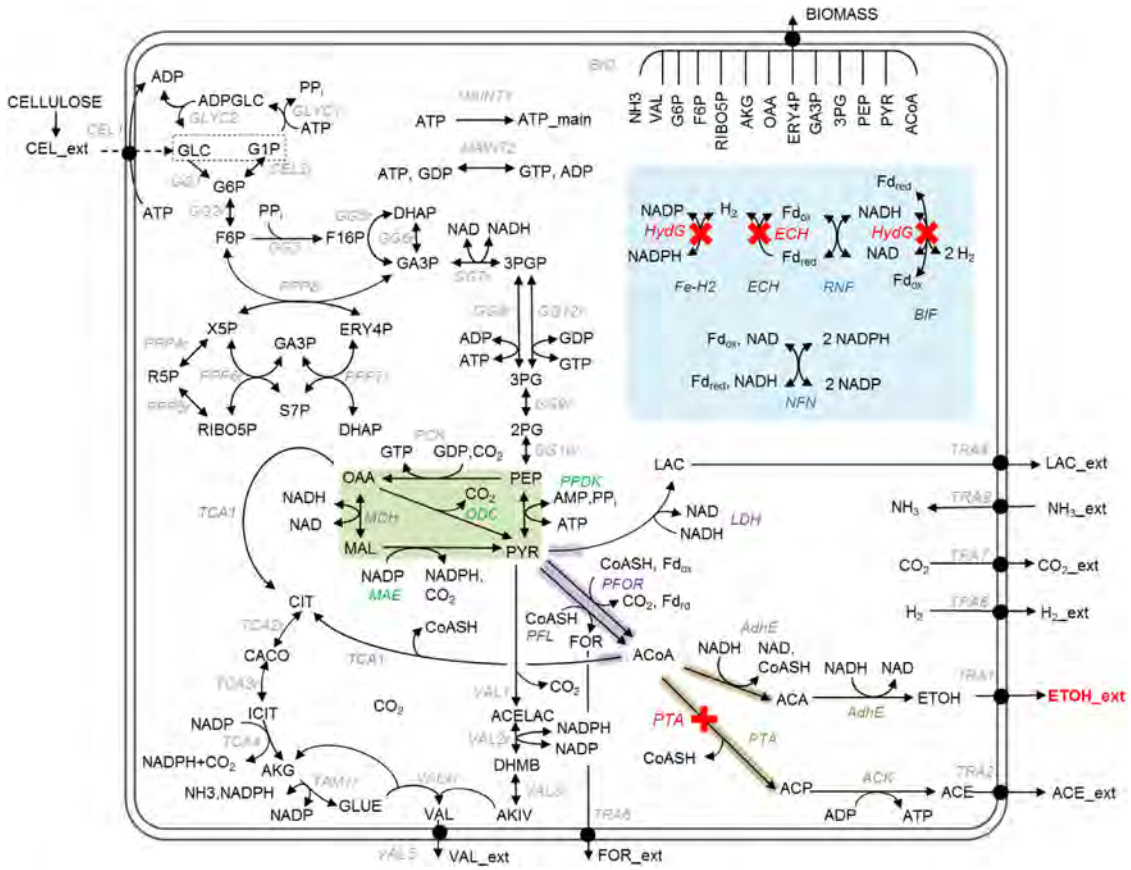

Fig. 1. The central metabolic network of *C. thermocellum*. Genetic modifications investigated in this study are marked with a red X. Reactions which contribute to metabolite nodes of interest are highlighted. Pyruvate phosphate dikinase (PPDK), oxaloacetate decarboxylase (ODC), and malic enzyme (MAE) contribute to →PYR (green box). Pyruvate formate lyase (PFL), pyruvate ferredoxin oxidoreductase (PFOR), and lactate dehydrogenase (LDH) contribute to PYR→ (purple box). ACoA→ (brown box) consists of alcohol dehydrogenase (AdhE), phosphotransacetylase (PTA), and citrate synthase (TCA1). The redox pathway is highlighted in the blue box. Fd_{rd}→ consists of the Ni–Fe energy conserving hydrogenase (ECH), the Rnf-type NADH:Fd oxidoreductase (RNF), the NADH-Fd_{rd}:$NADP^+$ oxidoreductase (NFN), and the NADH-Fd_{rd} bifurcating hydrogenase (BIF). The →H_2 node includes ECH, BIF, as well as the Fe–Fe NADPH-depenent hydrogenase (Fe–H_2). (For interpretation of the references to color in this figure legend, the reader is referred to the web version of this article.)

such as RNF or NFN, an Fe–Ni energy conservation hydrogenase (ECH), and several Fe–Fe hydrogenases which are activated by HydG (Fig. 1). A full list of reactions with stoichiometry is included in the Supplementary Materials.

2.7. Elementary mode analysis

From the construction of the *C. thermocellum* metabolic network, the mass balance for intracellular metabolites can be written as:

$$\frac{d\mathbf{c}}{dt} = \mathbf{S}\cdot\mathbf{r} - \mu\cdot\mathbf{c} \quad (4)$$

where **c** is the concentration vector of intracellular metabolites; **S** is the stoichiometric matrix whose rows and columns correspond to metabolites and reactions, respectively; **r** is the intracellular flux vectors ($r_i \geq 0$ for irreversible reactions i); and μ is the dilution effect. At quasi-steady state, Eq. (4) can be simplified to:

$$\mathbf{S}\cdot\mathbf{r} = 0 \quad (5)$$

$$r_i \geq 0 \quad (6)$$

Elementary mode analysis (EMA) was applied to calculate all possible solutions **r**, called elementary modes (EMs) that satisfy Eq. (5), inequality (6), and an additional non-decomposability constraint. The constraint states that for any $\mathbf{EM}_1$ and $\mathbf{EM}_2$, S($\mathbf{EM}_1$) cannot be a subset of S($\mathbf{EM}_2$) and vice versa where S($\mathbf{EM}_1$) and S($\mathbf{EM}_2$) are indices of non-zero fluxes of $\mathbf{EM}_1$ and $\mathbf{EM}_2$, respectively (Trinh et al., 2009). EMs were calculated for the metabolic network of *C. thermocellum* DSM 1313 by using METATOOL (Pfeiffer et al., 1999; Kamp and Schuster, 2006).

2.8. Metabolic flux analysis

We calculated the metabolic flux distribution for *C. thermocellum* based on the measured fluxes of extracellular metabolites under a given condition. The flux distribution was determined by a non-negative, linear combination of EMs using Poolman et al.'s algorithm (Poolman et al., 2004), and briefly described below:

$$\mathbf{r} = \mathbf{EM}\cdot\mathbf{w} \quad (7)$$

where **r** is a *n*x1 flux vector; **EM** is a *nxk* EM matrix; and **w** ($\in \Re^+$) is a *k*x1 weighing factor vector. By using the measured flux vector $\mathbf{r}_m$ ($\mathbf{r}_m \subseteq \mathbf{r}$), **w** can be calculated as follows:

$$\mathbf{r_m} = \mathbf{EM_m}\cdot\mathbf{w} \quad (8)$$

$$\mathbf{w} = \mathrm{pinv}(\mathbf{EM_m})\cdot\mathbf{r_m} \quad (9)$$

where pinv($\mathbf{EM_m}$) is the Moore-Penrose pseudo inverse matrix of $\mathbf{EM_m}$ (*mxk*). The flux calculation errors were determined as follows:

$$\mathbf{error} = \frac{\|\mathbf{r}-\mathbf{r_m}\|}{\|\mathbf{r}\|} \quad (10)$$

One-at-a-time sensitivity (OATS) analysis was performed by systematically removing an individual reaction from the EM space

for a given genotype, calculating the flux distribution with the resulting EM space, and comparing the new calculated error to the error of the original flux distribution vector.

2.9. Metabolic flux ratio analysis

To quantitatively differentiate flux distributions at key metabolite nodes in the central metabolic network upon perturbations, we employed the metabolic flux ratio (METAFoR) analysis (Sauer et al., 1999; Szyperski et al., 1999). The metabolic flux ratio for an incoming flux(es) at node i ($MFR_{i\leftarrow}$) is defined as

$$MFR_{i\leftarrow} = \frac{r_{j,i\leftarrow}}{\sum_k r_{k,i\leftarrow}} \quad (11)$$

where $r_{j,i\leftarrow}$ is the incoming flux(es) of node i through reaction j. $MFR_{i\rightarrow}$ can be defined similarly where the outgoing flux(es) of node i ($r_{j,i\rightarrow}$) is represented with the opposite arrow. Given the significant overflow metabolism in *C. thermocellum*, we are interested in carbon and electron fluxes directly to ethanol as well as upstream of ethanol synthesis. The key branch points in focus here are (i) conversion of PEP to pyruvate ($\rightarrow$PYR) via pyruvate phosphate dikinase (PPDK), oxaloacetate decarboxylase (ODC), and malic enzyme (MAE), with ODC and MAE jointly considered, (ii) recycling reduced ferredoxin ($Fd_{rd}\rightarrow$) through the Ni–Fe energy conserving hydrogenase (ECH), the Rnf-type NADH:Fd oxidoreductase (RNF), the NADH-Fd_{rd}:$NADP^+$ oxidoreductase (NFN), and the NADH-Fd_{rd} bifurcating hydrogenase (BIF), (iii) production of hydrogen ($\rightarrow H_2$) through ECH and BIF as well as the Fe–Fe NADPH-dependent hydrogenase (Fe–H_2), (iv) consumption of pyruvate (PYR$\rightarrow$) through pyruvate formate lyase (PFL), pyruvate: ferredoxin oxidoreductase (PFOR), and lactate dehydrogenase (LDH), and (v) acetyl-CoA flux (ACoA$\rightarrow$) to alcohol dehydrogenase (AdhE), phosphotransacetylase (PTA), and citrate synthase (TCA1) for ethanol, acetate, and cell mass production, respectively.

The workflow for integrating the experimental flux measurements to metabolic network analysis to elucidate reaction bottlenecks is shown in the Supplementary Fig. S1.

3. Results

3.1. Quantitative analysis of cellular phenotypic states of C. thermocellum

We first characterized the *C. thermocellum* strain DSM1313 Δ*hpt* (henceforth denoted "parent strain"). Similar to literature reports, the parent strain produced a mixture of fermentative products and amino acids (with valine as the most dominant) (Fig. 2A) with a good carbon recovery (Fig. 2B, Table 2). Due to the mixed acid fermentation, the ethanol yield (0.16 ± 0.01 g ethanol/g cellobiose) was low, as expected.

From the time-dependent concentration data, we extracted experimental fluxes for measured metabolites (Table 2), and calculated the metabolic flux distribution of the parent strain (Supplementary Table S2). Linear regression between the experimental and calculated fluxes gave an excellent fit ($R^2 = 0.96$, Supplementary Fig. S2A), indicating that the calculated flux distribution vector is a reasonable assessment of the central metabolism of *C. thermocellum*. In the subsequent sections, flux distributions of various *C. thermocellum* strains were calculated for quantitative analysis of their cellular physiological states, and were used to identify reaction bottlenecks hindering efficient ethanol production.

We used METAFoR analysis to examine the resulting flux distribution at key nodes more closely. Flux from pyruvate is determined directly by monitoring formate and lactate production. Additionally, the fate of acetyl-CoA in our model is determined by fermentation products and cell mass. However, the flux to pyruvate from PEP and flux through the redox pathways are only constrained by H_2 production which might not be effectively

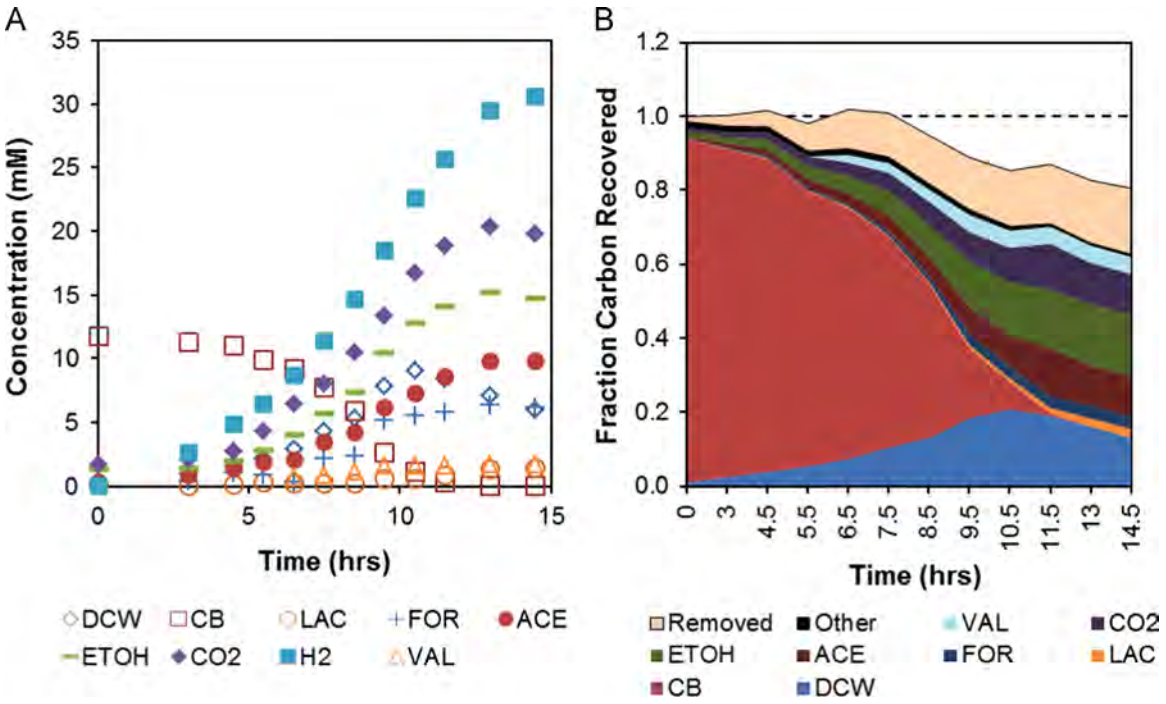

Fig. 2. (A) A concentration profile for the major metabolic end-products of the parent strain in a representative batch fermentation. (B) A representative carbon-balance applied throughout a parent strain batch fermentation. "Removed" indicates carbon removed during sampling while "other" consists of trace amino acids, mostly alanine and isoleucine. Abbreviations: CDW: cell dried weight; CB: cellobiose; LAC: lactate; FOR: formate; ACE: acetate; ETOH: ethanol; CO_2: carbon dioxide: H_2: hydrogen; and VAL: valine.

constrained and require additional experimental evidence (e.g., enzyme activities and proteomics). The best fit of experimental fluxes onto the EM space predicts that over 99% of flux to pyruvate proceeds through ODC and MAE combined, with the small remainder proceeding through PPDK (Fig. 3B). One-at-a-time sensitivity (OATS) analysis shows no effect when the malate shunt is deleted (Table 3), but this calculated flux distribution is consistent with high enzymatic activity in crude cell extracts (Zhou et al., 2013).

For H_2 flux, the best fit predicts over 90% proceeds through the ECH hydrogenase. This observation makes sense because, under high gas flow rate that was used in the experiments, the soluble H_2 was low and hence ECH was probably the major hydrogenase used in a thermodynamically favorable reaction. Since the network has many local redundancies around H_2 to allow for meaningful stoichiometric analysis for the parent strain, we also performed the OATS analysis to investigate the network structure's ability to give equivalent solutions. The results show that individual deletions of ECH, RNF, NFN, Fe–H_2, or BIF have no effect on the error of the

Table 2
Experimentally determined growth rates, metabolic fluxes, and yields per cellobiose for selected fermentative products for the parent, Δ*hydG*, Δ*hydG* Δ*ech*, and Δ*hydG* Δ*pta-ack* strains. Experimental data were obtained through pH controlled bioreactors. n.d. – Not detected.

Fermentation parameters	Parent	Δ*hydG*	Δ*hydG* Δ*ech*	Δ*hydG* Δ*pta-ack*
μ (hr^{-1})	0.33 ± 0.01	0.24 ± 0.02	0.22 ± 0.02	0.16 ± 0.02
Ethanol yield (g/g)	0.16 ± 0.01	0.19 ± 0.01	0.32 ± 0.04	0.25 ± 0.01
Maximum ethanol titer (g/L)	0.63 ± 0.03	0.79 ± 0.01	1.27 ± 0.05	1.01 ± 0.07
Carbon balance (% recovery)	90.5 ± 1.6	79.3 ± 1.6	89.9 ± 9.2	83.5 ± 4.1
Experimental flux (mmol species/gDCW/hr)				
$r_{CB\ up}$	3.58 ± 0.16	3.43 ± 0.25	3.33 ± 0.62	2.42 ± 0.05
r_{ETH}	4.19 ± 0.10	4.96 ± 0.24	7.95 ± 1.37	4.65 ± 0.25
r_{ACE}	2.63 ± 0.86	2.24 ± 0.57	0.67 ± 0.17	0.53 ± 0.21
r_{CO_2}	6.82 ± 0.01	7.25 ± 0.11	6.80 ± 1.01	5.29 ± 0.50
r_{FOR}	1.77 ± 0.01	1.22 ± 0.60	3.01 ± 0.56	0.74 ± 0.06
r_{H_2}	7.86 ± 0.38	9.11 ± 0.84	0.58 ± 0.06	3.17 ± 0.84
r_{VAL}	0.78 ± 0.12	0.35 ± 0.01	0.31 ± 0.01	0.55 ± 0.07
r_{LAC}	0.18 ± 0.01	n.d.	0.05 ± 0.01	0.03 ± 0.01

Table 3
One-at-a-time sensitivity (OATS) analysis for select reactions. *n/a* designates reactions which were removed prior to sensitivity analysis due to genotype.

		% Change in fitting error upon reaction removal			
Nodes of interest	Reactions	Parent	Δ*hydG*	Δ*hydG* Δ*ech*	Δ*hydG* Δ*pta-ack*
→PYR	MAE + ODC	0	0	0	0
	PPDK	0	0	0	0
PYR→	PFOR	228	163	583	288
	PFL	28	4	245	10
Electrons→	ECH	0	170	n/a	113
	Fe-H2	0	n/a	n/a	n/a
	BIF	0	n/a	n/a	n/a
	RNF	0	0	32	0
	NFN	0	0	0	0
Products→	Cell growth	16	11	31	13
	ETOH_out	114	71	764	246
	ACE_out	286	176	226	123
	CO2_out	309	221	717	374
	FOR_out	28	4	245	10
	H2_out	267	170	n/a	113

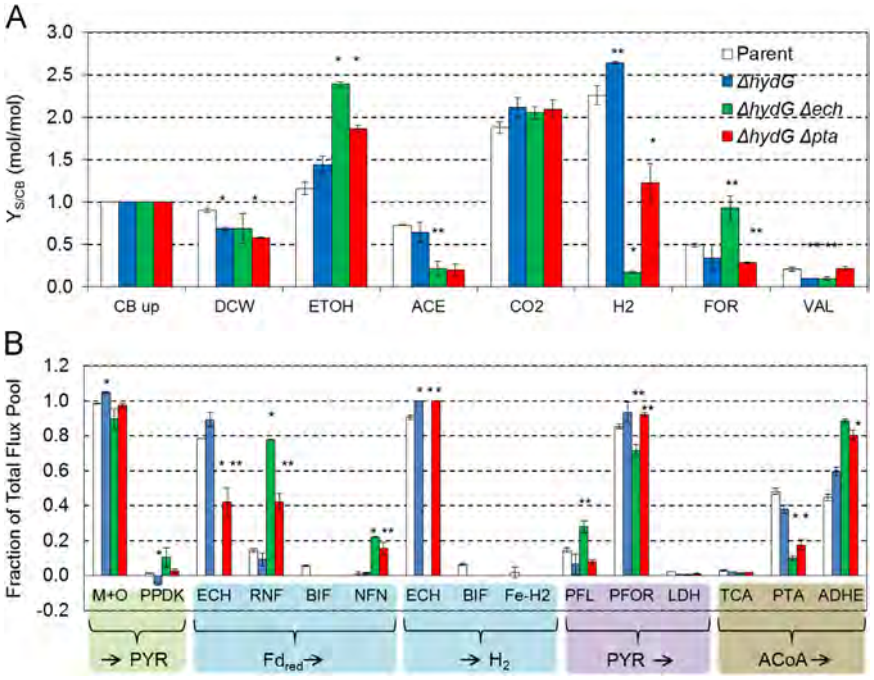

Fig. 3. (A) Experimental yields of major fermentative products on cellobiose for different genotypes. (B) Fraction of contribution of fluxes through specific metabolic nodes via METAFoR analysis for different genotypes. The groups are based on the metabolic nodes to which they contribute (Methods). Abbreviations: M + O, malic enzyme and oxaloacetate decarboxylase are collectively considered; PPDK, pyruvate phosphate dikinase; ECH, Ni–Fe Ech-type hydrogenase; RNF, NADH:Fd oxidoreductase; NFN, NADH-Fd_{rd}:$NADP^+$ oxidoreductase. BIF, bifurcating hydrogenase; Fe–H_2, NADPH dependent Fe–Fe hydrogenase; PFL, pyruvate formate lyase; PFOR, Pyruvate:Fd oxidoreductase; LDH, lactate dehydrogenase; TCA, citrate synthase (towards cell mass); PTA, acetate synthesis; and ADHE, ethanol synthesis. In both panels, student t-test significance compared to the parent strain is reported by asterisks, i.e., '*' for p-value < 0.01, and '**' for p-value < 0.05.

experimental data fitting (Table 3). This suggests that for the wildtype the redundancies in the redox pathway can compensate for individual gene deletions, and that genetically perturbing the system is necessary to obtain additional insights.

3.2. Metabolic model illustrates robust redox metabolism of *C. thermocellum*

3.2.1. Effect of partial deletion of hydrogen production

We characterized previously constructed strains with disrupted H_2 production in order to elucidate the effect of redox perturbation on *C. thermocellum* metabolism and ethanol production (Biswas et al., 2015). The first characterized mutant was the Δ*hydG* strain containing a disruption of the maturase enzyme complex, which inactivates the three Fe–Fe hydrogenases in *C. thermocellum* (Feinberg et al., 2011; Mulder et al., 2011) (Fig. 1). This strain also acquired a spontaneous mutation in the bifunctional alcohol/aldehyde dehydrogenase *adhE*, which allowed it to not only utilize NADH as an electron donor for acetaldehyde reduction to ethanol, but also NADPH. Deletion of *hydG* caused a 40% drop in the specific growth rate compared to the parent strain, and a lower yield of cell mass on cellobiose (Table 2). While the cellobiose uptake flux was minimally affected, the ethanol flux and yield on cellobiose increased 18% and 24%, respectively, and this slight increase in ethanol production was accompanied by a corresponding drop in acetate production (Fig. 3A), presumably due to greater electron availability for ethanol synthesis while lowering the acetyl-CoA pool used for acetate production.

Most interestingly, H_2 yield increased ~17% compared to the parent strain (Fig. 3A), which resulted in a very limited increase in ethanol production. This phenotype was unexpected and conflicts with previous reports of serum bottle cultures of the Δ*hydG* strain having a significant drop in H_2 yield (Biswas et al., 2015). This discrepancy can be explained by culture conditions, as we used a venting mechanism to measure gas concentrations in real-time and controlled pH, which prevents accumulation of H_2 and likely increases flux through the Ech hydrogenase.

To gain insights into the redox metabolism of *C. thermocellum*, we examined the flux distributions of the Δ*hydG* strain (Supplementary Table S2), which matched well with the experimental data (R^2=0.99, Supplementary Fig. S2B). A parametric plot of normalized flux distributions with respect to the cellobiose uptake fluxes shows no significant difference between the parent and Δ*hydG* strains (R^2=0.98, Fig. 4A). Outliers of this plot demonstrate the discrepancies of fluxes between the parent strain and the mutants. The only significant outlier was the NADPH-dependent AdhE* reaction, which is known not to be active in the parent strain (Lamed and Zeikus, 1980). Additionally, METAFoR analysis suggests that the malate shunt was still the major pathway to channel the carbon flux from PEP to pyruvate, and the fate of acetyl-CoA was minimally affected by the deletion of *hydG* (Fig. 3B). METAFoR analysis also shows that H_2 production can be compensated by the major ECH hydrogenase activity for effective electron shuttling in the absence of HydG-related enzyme activity. OATS analysis shows that removal of ECH from the Δ*hydG* network leads to a dramatic 170% change in error (Table 3).

3.2.2. Effect of complete deletion of hydrogen production

To characterize a dramatic push of electron flux towards enhanced ethanol production, we investigated the dual deletion Δ*hydG* Δ*ech* strain. The results show this mutant produced little H_2 and enhanced ethanol yield by 2.1 fold, while having similar growth characteristics as the Δ*hydG* strain (Table 2). Similar to the phenotype of the Δ*hydG* strain, the increase in ethanol production of the Δ*hydG* Δ*ech* strain was accompanied by decreased acetate production. However, one striking phenotype was that the formate yield, not the lactate yield, increased two-fold (Fig. 3A).

To elucidate how the Δ*hydG* Δ*ech* strain changed its metabolism to balance redox reactions, we calculated and analyzed the metabolic flux distribution (Supplementary Table S2). The distribution matched well with the experimental data (R^2=0.99, Supplementary Fig. S2C). Fig. 4B shows the significant discrepancies between the parent and the Δ*hydG* Δ*ech* strain (R^2=0.82). The outliers in this plot can be classified into two distinct groups, one associated with both carbon and electron fluxes (i.e., NADPH-dependent AdhE*, total ethanol production, PTA, and PFL) and the other associated with only electron fluxes (i.e., RNF, NFN, ECH, and total H_2 production). METAFoR analysis on the flux distribution of the Δ*hydG* Δ*ech* strain further revealed the dramatic restructuring of redox metabolism. The calculated share of reduced ferredoxin through the RNF reaction increased four-fold compared to the parent strain, whereas the flux through the NFN reaction, which was practically inactive in the parent strain, increased to account for 20% of the reduced ferredoxin recycling (Fig. 3B). This increase in NAD(P)H availability allowed for ethanol production to increase to 80% of the total flux through acetyl-CoA, and was matched by a drop in acetate production. Interestingly, ethanol yield only reached 59% of the theoretical limit while hydrogenase activities were diminished.

In summary, the complete disruption of H_2 production provided an effective means to increase flux of reducing equivalents to ethanol. This significant perturbation might have caused accumulation of reducing equivalents and hence triggered a regulatory mechanism for redox balancing where cells diverted pyruvate to

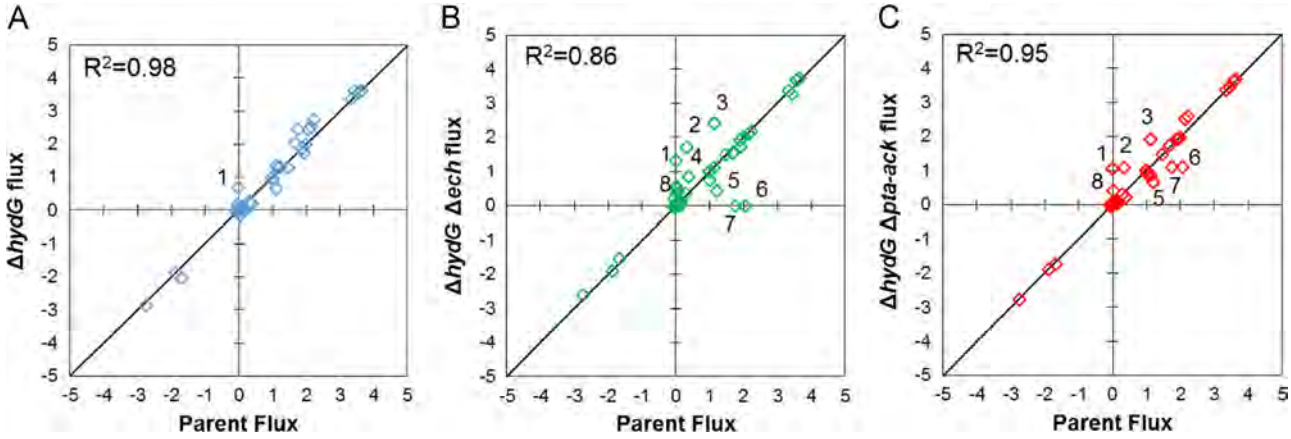

Fig. 4. Parametric plots of flux distributions between (A) the parent and Δ*hydG* strains, (B) the parent and Δ*hydG* Δ*ech* strains, and (C) the parent and Δ*hydG* Δ*pta-ack* strains. Reaction outliers are labeled as (1) NAPDH-dependent adhE* activity, (2) RNF, (3) ethanol export, (4) PFL, (5) acetate export, (6) ECH, (7) hydrogen export, and (8) NFN.

acetyl-CoA through the redox neutral PFL reaction instead of the reduced ferredoxin-generating PFOR reaction. This undesirable loss of reducing equivalents lessened the potential ethanol yield. The effect of this bifurcation at the pyruvate node on redox balance and ethanol production is further investigated in Section 3.4.

3.3. *The metabolic model encompasses several phenotypes*

As an additional assessment of our model's predictive capability, we constructed and characterized the Δ*hydG* Δ*pta-ack* strain which has perturbations designed to route carbon and electrons toward ethanol production with reduced production of H_2 and acetate. The results show that the Δ*hydG* Δ*pta-ack* strain achieved a 61% increase in the ethanol yield (Fig. 3A) while its growth rate decreased compared to the parent strain and the aforementioned Δ*hydG* strain by 50% and 30%, respectively (Table 1). This decreasing trend carried over to the cellobiose uptake rate, acetate production rate, and H_2 production rate (Table 2). The decreased growth rate and cell mass yield, with respect to the parent strain, could be attributed to the lack of ATP synthesis via substrate level phosphorylation through the *pta-ack* reaction pathway. In the Δ*hydG* Δ*pta-ack* strain, the lack of acetate production helped increase carbon flux from the acetyl-CoA node towards ethanol production, while also increasing flux of reducing equivalents (Fig. 3A). The need to balance carbon and electron fluxes to ethanol also translated to a 72% decrease in formate production, compared to the parent strain.

Like the aforementioned mutants, the calculated flux distribution matched experimental data well (R^2=0.96, Supplementary Fig. S2D), and when parametrically compared to the parent strain, one can quickly see a similar pattern of outlier reactions as seen in the Δ*hydG* Δ*ech* strain (Fig. 4C). The most prominent outliers focused again on carbon fluxes (i.e., NADPH-dependent AdhE*, total ethanol production, and PTA) and the electron fluxes (e.g., RNF, NFN, ECH, and total H_2 production). To elaborate on this point, METAFoR analysis (Fig. 3B) shows how the Δ*hydG* Δ*pta-ack* strain recycled reduced ferredoxin equivalently through the ECH and RNF reactions, as opposed to the parent strain predominately

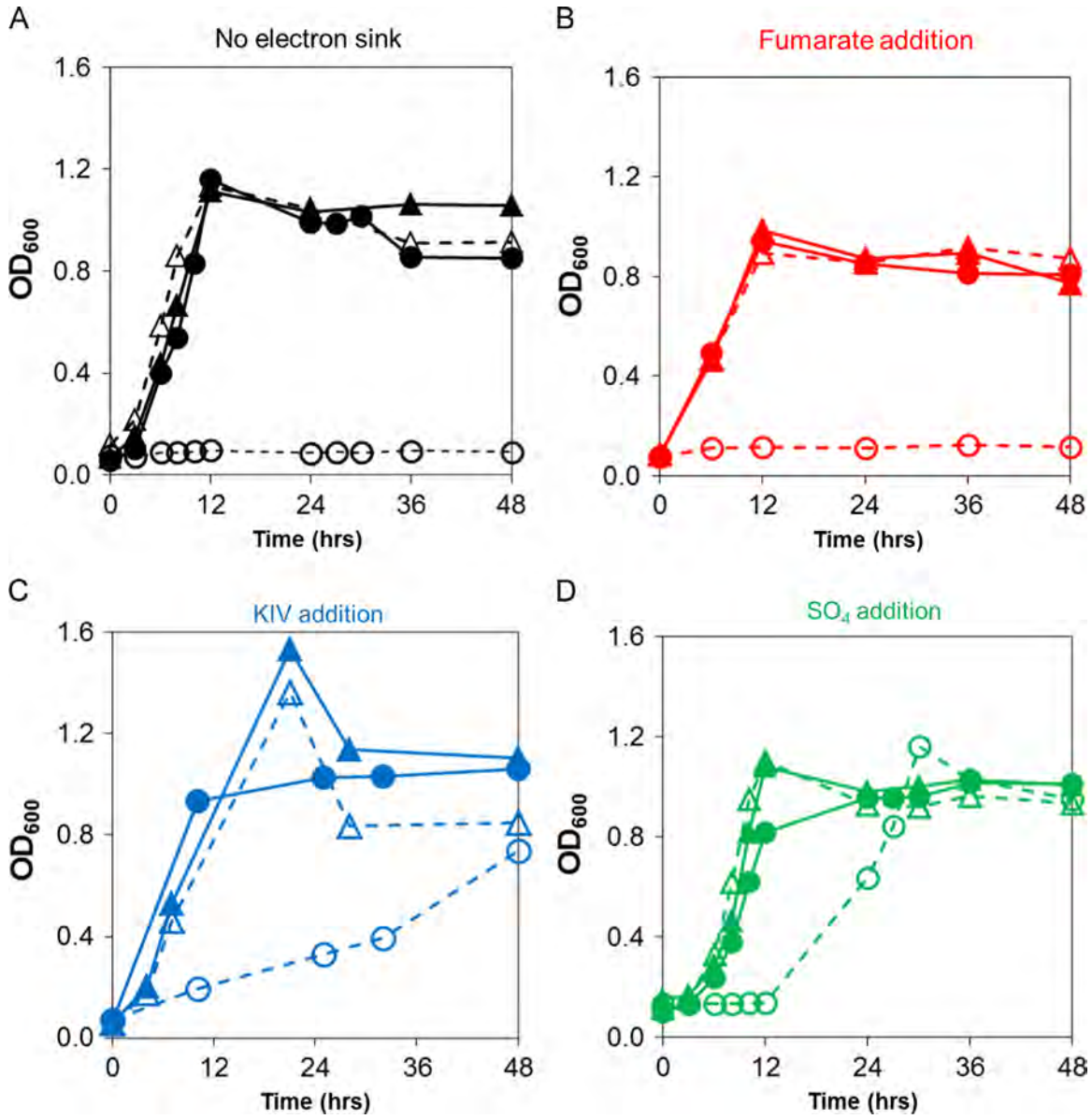

Fig. 5. Growth characteristics of parent strain (triangles) and Δ*hydG* Δ*ech* (circles) in MTC media (filled symbols) or MTC with the PFL inhibitor hypophosphite (open symbols). To investigate redox bottlenecks, no additional electron sink (A), 20 mM fumarate (B), 20 mM 2-ketoisovalerate (C), or 2 g/L total sulfate (D) were included in the medium to probe NADH, NAD(P)H, and Fd_{rd}, respectively.

utilizing ECH. Furthermore, the NFN flux increased to about 14% of the total reduced ferredoxin recycling in the Δ*hydG* Δ*pta-ack* strain. The increase in RNF and NFN fluxes provided the NAD(P)H necessary for ethanol production, and as expected the share of acetyl-CoA going to ethanol production increased over 60% compared to the parent strain (Fig. 3B).

Taken all together, the model elucidates how *C. thermocellum* adjusts electron and carbon fluxes when its redox metabolism is perturbed towards ethanol production. These results give confidence in the model structure and any further phenotypic predictions.

3.4. Elucidating the redox bottlenecks hindering ethanol production

While the energy and redox perturbations enhanced ethanol flux, the ethanol yield was still low, only reaching 60% of the theoretical limit. This result indicates that the capacity for ethanol flux might still be limiting ethanol production. Since *C. thermocellum* employs multiple metabolic control valves, such as flux bifurcation at the pyruvate node via PFL and PFOR and/or distribution of electron fluxes via NFN, RNF, BIF, and the Fe–H_2 reactions, we used EMA to simulate additional redox-disrupted genotypes to identify key bottlenecks hindering high-yielding ethanol production.

3.4.1. PFL is vital for redox balancing when hydrogenases are inactive

Relative to the parent strain, a 70% increase in the flux to formate in the Δ*hydG* Δ*ech* mutant suggests that accumulation of reduced ferredoxin results in a decrease in PFOR flux and increase in PFL flux. The importance of formate production is also apparent in the OATS analysis for the Δ*hydG* Δ*ech* network (Table 3). To further examine this observation, we investigated whether additional deletion of *pfl* in the Δ*hydG* Δ*ech* mutant would cause a redox imbalance which inhibits cell growth.

In silico results, via EMA, show that the Δ*hydG* Δ*ech* Δ*pfl* strain had zero EMs that supported cell growth (Supplementary Fig. S3A). To date, this strain has not been constructed. However, hypophosphite (HPP) is a known PFL inhibitor (Rydzak et al., 2014) and can be used to experimentally eliminate PFL activity. Therefore, we tested this genotype experimentally by growing the Δ*hydG* Δ*ech* strain in the presence of 6 mM HPP. While HPP had no effect on the growth of the parent strain, we were able to confirm the model's prediction of growth inhibition when HydG, Ech, and Pfl were inactivated (Fig. 5A). These results suggest that without the redox neutral relief valve of PFL, the lack of H_2 production causes a redox imbalance within the metabolism of *C. thermocellum* that eliminates cell growth.

3.4.2. Probing redox bottlenecks via external electron acceptors

To investigate if growth could be recovered when Pfl is inhibited in the Δ*hydG* Δ*ech* strain, we simulated the addition of alternative electron consumption pathways into the model (see Table S1 for pathway description.) The electron sinks were chosen to test the accumulation of the major electron carrying species: (1) fumarate was tested for NADH recycling due to the presence of a fumarate reductase domain (Clo1313_3018) and a hypothetical protein with similarity to succinate dehydrogenase (Clo1313_2640); (2) 2-ketoisovalerate (KIV) was tested for NAD(P)H recycling due to experimental evidence of isobutanol production in *C. thermocellum* (Holwerda et al., 2014); and (3) sulfate was tested for ferredoxin recycling as at least one of the steps to sulfate reduction is ferredoxin dependent (Feinberg et al., 2011). Reactions are included in Table S1. *In silico* results demonstrate that addition of any single electron sink pathway into the Δ*hydG* Δ*ech* Δ*pfl* metabolic network restored the phenotypic space to the same area and yield ranges as the parent or Δ*hydG* strain (Supplementary Fig. S3). To test these phenotypes experimentally, we investigated the growth behavior of the parent versus Δ*hydG* Δ*ech* strains in the presence of various electron sinks, with and without inhibition of PFL by HPP.

First, the parent strain (positive control) could grow with or without the HPP inhibition regardless of supply of external electron acceptors (Fig. 5A), as expected. For the Δ*hydG* Δ*ech* strain, exogenous addition of 40 mM fumarate was unable to restore growth with PFL inhibition (Fig. 5B). This result indicates that (i) there is not an accumulation of NADH and/or (ii) the annotated fumarate reductase was not active. It should be noted that the level of fumarate addition was non-toxic because the parent strain and Δ*hydG* Δ*ech* strains grew under conditions without HPP. Furthermore, addition of 40 mM KIV led to slight growth (Fig. 5C) and isobutanol production (data not shown) after two days. This result indicates that accumulation of NAD(P)H could be occurring.

Interestingly, the normal levels of sulfate in MTC media (1 g L^{-1} Na_2SO_4) were not sufficient to allow growth of Δ*hydG* Δ*ech* Δ*pfl*. However, addition of extra sulfate (2 g L^{-1} Na_2SO_4 total) into the culture medium was able to bring the maximum OD_{600} to levels comparable to the control (Fig. 5D) after a lag phase. This result suggests that reduced ferredoxin is the species most likely accumulating, causing the lethal electron imbalance.

Collectively, perturbation of redox metabolism was effective for pushing electron and carbon fluxes towards the production of reduced metabolites e.g. ethanol. Accumulation of reduced ferredoxin triggered the bifurcation at the pyruvate node to balance redox potentials. Thus, either transfer of electrons from ferredoxin to NAD(P)H or electron pulling by the native ethanol pathway was not sufficient to maximize ethanol production. This mechanism was supported by the observed high formate flux in the Δ*hydG* Δ*ech* strain as well as *in silico* and *in vivo* probing of redox bottlenecks in *C. thermocellum* using different external electron acceptors.

3.5. Design of optimal genotype of C. thermocellum for high-yield ethanol production

With the trained metabolic model, we next applied EMA to analyze the network structure and give insights for rational strain design (Trinh et al., 2009).

3.5.1. Additional modifications are necessary to constrain C. thermocellum phenotype

To explain why the above metabolic engineering strategies were not sufficient to achieve high-ethanol yields, we used EMA to qualitatively assess phenotypic spaces of the parent, Δ*hydG*, Δ*hydG* Δ*ech*, and Δ*hydG* Δ*pta-ack* strains, solely based on the metabolic network structure. Table 4 summarizes the EM properties of each genotype while Fig. 6 compares the phenotypic spaces of the parent strain with the three mutant strains focusing on the 2-D projection of the ethanol versus cell mass yields on

Table 4
Elementary mode analysis for various *C. thermocellum* mutants.

Network characteristics	Parent	Δ*hydG*	Δ*hydG* Δ*ech*	Δ*hydG* Δ*pta-ack*
Total EMs	5202	2258	1148	816
ETH EMs	1982	1357	807	499
BIO EMs	3858	1478	718	558
Both EMs	1143	842	470	334
Range ETH (Cmol/Cmol)	0.000–0.667	0.000–0.667	0.000–0.667	0.000–0.667
Range BIO (Cmol/Cmol)	0.000–0.394	0.000–0.394	0.000–0.330	0.000–0.247

cellobiose. This representation is commonly used to qualitatively compare what phenotypes a metabolic network can feasibly attain given its stoichiometric structure. By definition, the experimental phenotypes of the wildtype or any knock-out mutant must fall within the phenotypic space predicted by the model unless new reactions are added to the network; otherwise, there is at least one error present in the model structure.

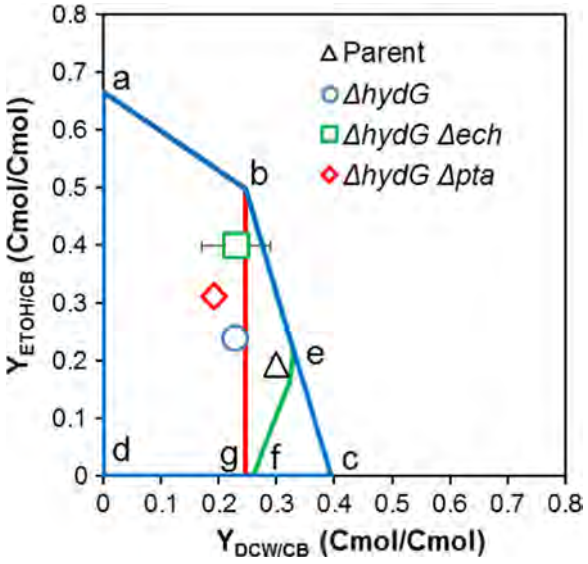

Fig. 6. The 2-D phenotypic spaces of ethanol versus cell mass yields on cellobiose for various genotypes. The phenotypic spaces (or convex hull) are encompassed by the areas 'abcd' for the parent and Δ*hydG* strains, 'abefd' for Δ*hydG* Δ*ech* strain, and 'abgd' for Δ*hydG* Δ*pta-ack* strain. Symbols within these areas are experimental yields.

When examining the presented strains, an immediately noticeable result is the similarity of the phenotypic spaces. The Δ*hydG* strain had the same space boundaries as the parent strain (the area 'abcd', Fig. 6), while the Δ*hydG* Δ*ech* strain shows a slightly contracted space (the area 'abefd') with regards to the cell mass yield. Since cellobiose and dry cell weight have equivalent oxidation states, the contracted space can be attributed to the lack of carbon-free electron disposal in the form of hydrogen production requiring the synthesis of reduced carbon compounds such as ethanol and lactate to balance redox. This flux of carbon to other reduced products limits the yield of dry cell weight. The Δ*hydG* Δ*pta-ack* strain exhibits a truncated boundary on the cell mass yield axis (the area 'abgd') which can be attributed to a lower ATP availability for cell synthesis due to a lack of substrate-level phosphorylation by *pta-ack*.

Most importantly, for each genotype, the admissible range of ethanol still stretched from 0.00 to 0.67 (Cmol/Cmol). This indicates that there are accessible phenotypic states for these strains that do not produce any ethanol; the existence of the undesired EMs in these strains helps explain why they did not reach high ethanol yields experimentally (Table 2). It should be noted that each phenotypic space represent the metabolic capabilities of each genotype at quasi steady state. Under a given operating condition, each genotype will occupy a point within its own space, i.e., symbols in Fig. 6 designate the phenotypic states of the parent strain and its mutants under our characterized conditions.

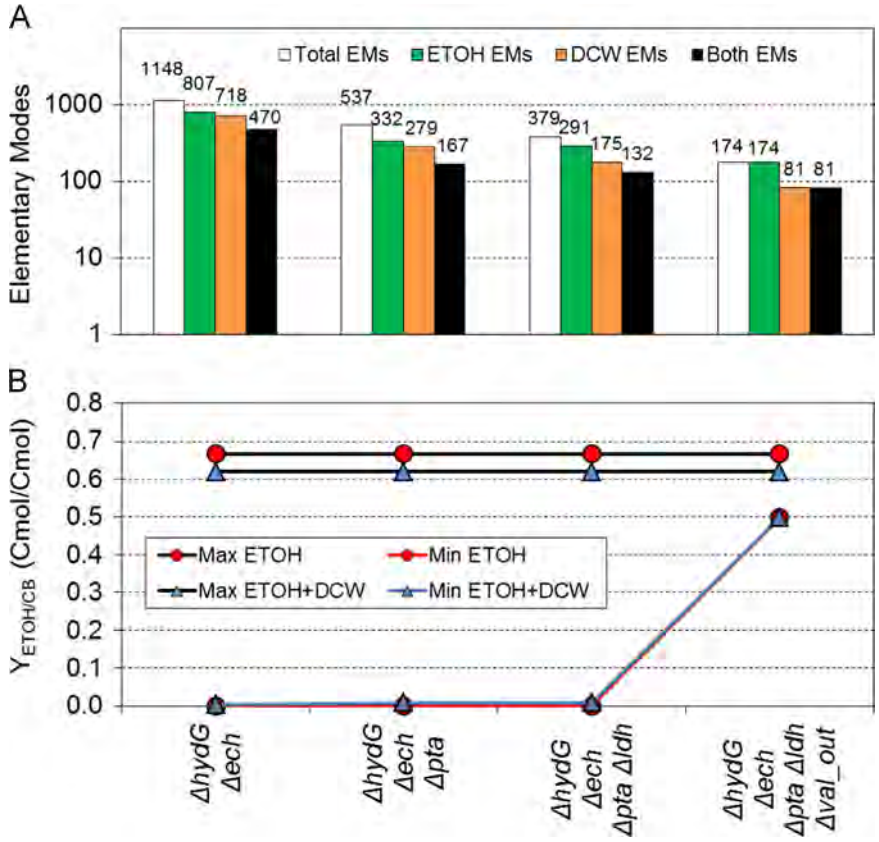

Fig. 7. Application of MMF algorithm to identify the optimal genotype of *C. thermocellum* for high-yield ethanol production. (A) Effect of reaction deletions on the total EMs, ethanol-producing EMs, cell mass-producing EMs, and coupled ethanol- and cell mass-producing EMs. (B) Effect of reaction deletions on minimum and maximum yields of ethanol and cell mass on cellobiose.

3.5.2. Metabolic model predicts feasibility of high-ethanol yielding phenotype

We investigated the ability of the central metabolic model to describe a high ethanol yielding (> 75% theoretical maximum) phenotype by performing the Minimal Metabolic Functionality (MMF) algorithm (Trinh et al., 2008). The MMF method constrains the phenotypic space by iteratively performing gene deletions *in silico*, aiming to reduce the total number of elementary modes and the accessible range of the desired product. When running the MMF algorithm, we opted to start with the Δ*hydG* Δ*ech* genotype, since an increase in ethanol yield was observed in that strain, the dual NADH/NADPH activity has been shown for ethanol synthesis, and genetic manipulation in *C. thermocellum* is a bottleneck in strain design (Tripathi et al., 2010; Mohr et al., 2013). Fig. 7 presents the stepwise progress of the MMF algorithm on the number of EMs describing the genotype, as well as the range of ethanol yields. While simulating a Δ*hydG* Δ*ech* Δ*pta-ack* strain reduced the total number of elementary modes by about half, and simulating Δ*hydG* Δ*ech* Δ*pta-ack* Δ*ldh* reduced the total EMs by another 40%, the range of ethanol yield was not constrained (Fig. 7). However, simulating Δ*hydG* Δ*ech* Δ*pta-ack* Δ*ldh* Δval_{out} brought the ethanol yield range to 0.50–0.67 (Cmol ETOH/Cmol CB) for non-growth associated production and 0.50–0.62 (Cmol ETOH/Cmol CB) for growth-associated ethanol production, while reducing the total number of EMs again by over half. This result invites the hypothesis that central metabolism can be constrained to a high-yielding phenotypic space with only three additional gene deletions. The ability to delete or overexpress genes in *C. thermocellum* is a significant challenge in its own right (Guss et al., 2012; Mohr et al., 2013), and as such the construction of the optimal strain predicted here is beyond the scope of this report.

4. Discussion

We developed and validated a predictive, stoichiometric, central metabolic model of *C. thermocellum* for flux quantification to elucidate cellular phenotypes and rational strain design based on EMA. The model was able to illuminate how *C. thermocellum* dramatically shifts its cofactor recycling processes when exposed to significant energy and redox perturbations. In each of the mutants presented, a change from the parent strain central metabolism led to an increase in ethanol production. The proposed mechanism is an increase in conversion of reduced ferredoxin to NAD(P)H through NFN and RNF.

Our study reveals the major driving force in ethanol production is a need to balance redox metabolism, as opposed to the push of carbon flux. At the same time, the diverse routes for regeneration of oxidized electron carriers offer many different avenues for producing reduced products other than ethanol. For instance, in the Δ*hydG* strain, the results suggest that the reduced ferredoxin positively affects ECH flux since specific H_2 production increased without a significant change in the production of ethanol. Additionally, the Δ*hydG* Δ*ech* and Δ*hydG* Δ*pta-ack* strains had similar acetate yields, but the Δ*hydG* Δ*ech* strain had a 28% increase in ethanol yield compared to the Δ*hydG* Δ*pta-ack* strain (Fig. 3A).

The need to balance redox metabolism as a driving force is also intuitive when considering acetyl-CoA is made available by both PFOR and PFL reactions as well as the fact that the sum of PFOR and PFL fluxes is not significantly altered by genotype (Table S2). This suggests AdhE* activity is not acetyl-CoA limited. The experimental data suggests that regenerating reduced ferredoxin solely through PFOR is not sufficient to match the rate of cellobiose uptake and glycolysis. To compensate, pyruvate consumption is diverted from the stalling PFOR reaction towards the redox neutral PFL reaction (Fig. 3B), which is consistent with literature reports of conditions with disrupted H_2 synthesis (Rydzak et al., 2014; Biswas et al., 2015). The decrease in flux through PFOR can be attributed to rate-limitation at either (i) reduced ferredoxin recycling via NFN or RNF, or (ii) the push of NAD(P)H to ethanol synthesis (i.e. AdhE* activity).

It is worth noting the difference in H_2 production in the Δ*hydG* strain in serum bottles (Biswas et al., 2015) and the bioreactor studies presented here could be linked to inhibition of ECH activity and an increase in the activities of NFN and RNF. The calculated flux distribution for the Δ*hydG* Δ*ech* strain shows that NFN and RNF become highly active to compensate for diminished hydrogenase activity. Therefore, it is feasible to propose that the higher partial pressure of H_2 in serum bottle cultures increases the availability of NAD(P)H in the Δ*hydG* strain. Indeed, it has been shown that artificially increasing H_2 in the culture atmosphere leads to increased ethanol production (Rydzak et al., 2011). The hypothesis that H_2 inhibition is lower for ECH than the bifurcating hydrogenase or Fe–Fe hydrogenases could explain the higher H_2 yield in the parent strain serum bottle studies, since all hydrogenases should be actively present. In contrast, the only way that the Δ*hydG* Δ*ech* strain can recycle reduced ferredoxin is to produce NAD(P)H via RNF or NFN.

To further highlight the importance of redox balance, inhibiting PFL activity in the Δ*hydG* Δ*ech* strain causes growth to cease. This phenotype was predicted by our model and then confirmed in batch cultures. This effective genotype serves as a promising experimental condition to probe bottlenecks in redox cofactor recycling by use of exogenous electron sinks. We anticipated that the addition of fumarate would serve as a NADH probe and restore redox balance through succinate production. However, the fumarate study was inconclusive as the inability to restore growth could be due to a lack of fumarate reductase expression, lack of a fumarate transport protein, or an incorrect annotation of the fumarate reductase protein.

The inconclusive results from the fumarate study led to the use of KIV as a NAD(P)H probe. This gave more promising results, as growth was slowly able to recover, cellobiose was consumed in the process, and isobutanol was detected. The slow growth recovery clearly shows additional reducing equivalents can be recycled via KIV conversion to isobutanol. The slow rate of growth likely reflects a kinetic bottleneck in the conversion of reduced ferredoxin to NAD(P)H and/or low activity of KIV reductase, although isobutylaldehyde reduction kinetics or isobutanol toxicity cannot be ruled out.

The final electron sink, sulfate, was designed to probe the accumulation of reduced ferredoxin. After a lag phase, growth was recovered to a rate comparable to controls without HPP. The lag phase could be due to an adjustment in gene expression levels for greater sulfate reduction. These results allude to reduced ferredoxin being the main accumulating redox cofactor, which implies that re-oxidation of ferredoxin is a rate limiting step in the electron recycling pathway of *C. thermocellum*. Future experiments overexpressing these potential bottleneck enzymes should enhance ethanol production.

Our application of the MMF method to *C. thermocellum* revealed that elimination of H_2 production coupled with the removal of acetate and lactate synthesis as well as valine secretion effectively constrains the network to a high yielding ethanol phenotype (Fig. 7). It is worthwhile again to note that PFL is not included in this set of reaction deletions, as the model predicts that removing H_2 and formate production does not allow cell growth. While the MMF method seeks to find all reaction deletion sets that have the minimum size (i.e., cardinality) and exclude reactions downstream of a linear pathway (Trinh et al., 2009), it is possible to identify other unique sets with larger sizes by using the cMCS tool to achieve the same high yielding ethanol phenotype (Hädicke and Klamt, 2011). Due to many possible candidate design strains generated by the cMCS method (> 5000 for our network),

great care must be taken to screen out those that are not biologically relevant. Given the redox bottlenecks in reduced ferredoxin recycling, as previously discussed, simply deleting the above-mentioned genes might not immediately facilitate high ethanol productivity. Presumably, a directed evolutionary approach to select for faster growth or, more proactively, the intentional overexpression of NFN, RNF, and AdhE*, will be necessary for the designed strain to overcome metabolic obstacles and reach the desired, high ethanol yielding phenotype.

It should be emphasized that even though the model-driven approach presented in this study is powerful for strain design and optimization, validating the design is not a trivial task to implement in *C. thermocellum.* The main reasons are that genetic tools (e.g., gene deletion and expression) for *C. thermocellum* are not well established and native complex genetics are not well understood compared to those of the model organisms (e.g., *E. coli and S. cerevisiae*) despite significant progress made in very recent years (Guss et al., 2012; Olson and Lynd, 2012; Olson et al., 2015). It is certain that the development of the powerful genome editing tools like CRISPR/Cas9 (Wang et al., 2015) and siRNA (Tummala et al., 2003; Na et al., 2013) for *C. thermocellum,* if successful, will be beneficial for metabolic engineering of this organism for production of fuels and high-value chemicals from lignocellulosic biomass. Even though our metabolic model is constructed for the *C. thermocellum* DSM1313, different from the iSR432 model developed for *C. thermocellum* ATCC 27405 (Gowen and Fong, 2010; Roberts et al., 2010), the important features (e.g. the atypical glycolysis and a complete model of redox regulatory mechanisms) should be applicable to ATCC 27405, and hence their incorporation should improve the prediction of the iSR432 model.

In summary, our study accents the hypothesis that constricting electron flux contributes more than carbon redirection to ethanol production in *C. thermocellum*, and identifies bottlenecks in the redox metabolism hindering high ethanol yields. Rational strain design based on the MMF method and *in vivo* characterizations predict increasing flux through NFN, RNF, and/or AdhE* while eliminating acetate, lactate, H_2, and valine production is the most promising strategy for optimizing the production of ethanol. We envision that our trained metabolic model will be used to engineer *C. thermocellum* as a CBP platform to produce other reduced metabolites.

Acknowledgments

This research was supported as a subcontract by the BioEnergy Science Center (BESC), a U.S. Department of Energy Bioenergy Research Center funded by the Office of Biological and Environmental Research in the DOE Office of Science (DE-AC05-000R22725). The authors would like to thank Dr. Joe Bozell (the Center of Renewable Carbon, UTK) for use of the GC/MS instrument and Dr. Gary Sayler (the Center of Environmental Biotechnology, UTK) for use of the SRS UGA-300 Universal Gas Analyzer. We also thank Prof. Hans van Dijken for useful discussion.

Appendix A. Supplementary material

Supplementary data associated with this article can be found in the online version at http://dx.doi.org/10.1016/j.ymben.2015.10.004.

References

Argyros, D.A., Tripathi, S.A., Barrett, T.F., Rogers, S.R., Feinberg, L.F., Olson, D.G., Foden, J.M., Miller, B.B., Lynd, L.R., Hogsett, D.A., Caiazza, N.C., 2011. High ethanol titers from cellulose by using metabolically engineered thermophilic, anaerobic microbes. Appl. Environ. Microbiol. 77 (23), 8288–8294.

Biswas, R., Prabhu, S., Lynd, L.R., Guss, A.M., 2014. Increase in ethanol yield via elimination of lactate production in an ethanol-tolerant mutant of *Clostridium thermocellum*. PLoS One 9 (2), e86389.

Biswas, R., Zheng, T., Olson, D., Lynd, L., Guss, A., 2015. Elimination of hydrogenase active site assembly blocks H_2 production and increases ethanol yield in *Clostridium thermocellum*. Biotechnol. Biofuels 8 (1), 20.

Brown, S.D., Guss, A.M., Karpinets, T.V., Parks, J.M., Smolin, N., Yang, S., Land, M.L., Klingeman, D.M., Bhandiwad, A., Rodriguez Jr., M., Raman, B., Shao, X., Mielenz, J.R., Smith, J.C., Keller, M., Lynd, L.R., 2011. Mutant alcohol dehydrogenase leads to improved ethanol tolerance in *Clostridium thermocellum*. Proc. Natl. Acad. Sci. USA 108 (33), 13752–13757.

Carere, C., Rydzak, T., Verbeke, T., Cicek, N., Levin, D., Sparling, R., 2012. Linking genome content to biofuel production yields: a meta-analysis of major catabolic pathways among select H_2 and ethanol-producing bacteria. BMC Microbiol. 12 (1), 295.

Demain, A.L., 2009. Biosolutions to the energy problem. J. Ind. Microbiol. Biotechnol. 36 (3), 319–332.

Deng, Y., Olson, D.G., Zhou, J., Herring, C.D., Shaw, A.J., Lynd, L.R., 2013. Redirecting carbon flux through exogenous pyruvate kinase to achieve high ethanol yields in *Clostridium thermocellum*. Metab. Eng. 15, 151–158.

Ellis, L.D., Holwerda, E.K., Hogsett, D., Rogers, S., Shao, X., Tschaplinski, T., Thorne, P., Lynd, L.R., 2012. Closing the carbon balance for fermentation by *Clostridium thermocellum* (ATCC 27405). Bioresour. Technol. 103 (1), 293–299.

Feinberg, L., Foden, J., Barrett, T., Davenport, K.W., Bruce, D., Detter, C., Tapia, R., Han, C., Lapidus, A., Lucas, S., Cheng, J.-F., Pitluck, S., Woyke, T., Ivanova, N., Mikhailova, N., Land, M., Hauser, L., Argyros, D.A., Goodwin, L., Hogsett, D., Caiazza, N., 2011. Complete genome sequence of the cellulolytic thermophile *Clostridium thermocellum* DSM1313. J. Bacteriol. 193 (11), 2906–2907.

Gowen, C.M., Fong, S.S., 2010. Genome-scale metabolic model integrated with RNAseq data to identify metabolic states of *Clostridium thermocellum*. Biotechnol. J. 5 (7), 759–767.

Guss, A.M., Olson, D.G., Caiazza, N.C., Lynd, L.R., 2012. Dcm methylation is detrimental to plasmid transformation in *Clostridium thermocellum*. Biotechnol. Biofuels 5, 30.

Hädicke, O., Klamt, S., 2011. Computing complex metabolic intervention strategies using constrained minimal cut sets. Metab. Eng. 13 (2), 204–213.

Herrero, A.A., Gomez, R.F., 1980. Development of ethanol tolerance in *Clostridium thermocellum*: effect of growth temperature. Appl. Environ. Microbiol. 40 (3), 571–577.

Holwerda, E., Thorne, P., Olson, D., Amador-Noguez, D., Engle, N., Tschaplinski, T., van Dijken, J., Lynd, L., 2014. The exometabolome of *Clostridium thermocellum* reveals overflow metabolism at high cellulose loading. Biotechnol. Biofuels 7 (1), 155.

Kamp, A. v, Schuster, S., 2006. Metatool 5.0: fast and flexible elementary modes analysis. Bioinformatics 22 (15), 1930–1931.

Kridelbaugh, D.M., Nelson, J., Engle, N.L., Tschaplinski, T.J., Graham, D.E., 2013. Nitrogen and sulfur requirements for *Clostridium thermocellum* and *Caldicellulosiruptor bescii* on cellulosic substrates in minimal nutrient media. Bioresour. Technol. 130 (0), 125–135.

Kuyper, M., Toirkens, M.J., Diderich, J.A., Winkler, A.A., van Dijken, J.P., Pronk, J.T., 2005. Evolutionary engineering of mixed-sugar utilization by a xylose-fermenting Saccharomyces cerevisiae strain. FEMS Yeast Res. 5 (10), 925–934.

Lamed, R., Zeikus, J.G., 1980. Ethanol production by thermophilic bacteria: relationship between fermentation product yields of and catabolic enzyme activities in *Clostridium thermocellum* and *Thermoanaerobium brockii*. J. Bacteriol. 144 (2), 569–578.

Lynd, L.R., Laser, M.S., Bransby, D., Dale, B.E., Davison, B., Hamilton, R., Himmel, M., Keller, M., McMillan, J.D., Sheehan, J., Wyman, C.E., 2008. How biotech can transform biofuels. Nat. Biotechnol. 26 (2), 169–172.

Lynd, L.R., Van Zyl, W.H., McBride, J.E., Laser, M., 2005. Consolidated bioprocessing of cellulosic biomass: an update. Curr. Opin. Biotechnol. 16 (5), 577–583.

Mohr, G., Hong, W., Zhang, J., Cui, G.-z, Yang, Y., Cui, Q., Liu, Y.-j, Lambowitz, A.M., 2013. A targetron system for gene targeting in thermophiles and its application in *Clostridium thermocellum*. PLoS One 8 (7), e69032.

Mulder, David W., Shepard, Eric M., Meuser, Jonathan E., Joshi, N., King, Paul W., Posewitz, Matthew C., Broderick, Joan B., Peters, John W., 2011. Insights into [FeFe]-Hydrogenase Structure, Mechanism, and Maturation. Structure 19 (8), 1038–1052.

Na, D., Yoo, S.M., Chung, H., Park, H., Park, J.H., Lee, S.Y., 2013. Metabolic engineering of Escherichia coli using synthetic small regulatory RNAs. Nat. Biotech. 31 (2), 170–174.

Neidhardt, F.C., Ingraham, J.L., Schaechter, M., 1990. Physiology of the Bacterial Cell: A Molecular Approach. Sinauer Associates, USA.

Ng, T.K., Zeikus, J.G., 1982. Differential metabolism of cellobiose and glucose by *Clostridium thermocellum* and *Clostridium thermohydrosulfuricum*. J. Bacteriol. 150 (3), 1391–1399.

Nochur, S.V., Jacobson, G.R., Roberts, M.F., Demain, A.L., 1992. Mode of sugar phosphorylation in *Clostridium thermocellum*. Appl. Biochem. Biotechnol. 33 (1), 33–41.

Olson, D.G., Lynd, L.R., 2012. Transformation of *Clostridium thermocellum* by electroporation. Method Enzymol., 317–330.

Olson, D.G., Maloney, M., Lanahan, A.A., Hon, S., Hauser, L.J., Lynd, L.R., 2015. Identifying promoters for gene expression in *Clostridium thermocellum*. Metab. Eng. Commun., 0.

Ozkan, M., Desai, S.G., Zhang, Y., Stevenson, D.M., Beane, J., White, E.A., Guerinot, M. L., Lynd, L.R., 2001. Characterization of 13 newly isolated strains of anaerobic, cellulolytic, thermophilic bacteria. J. Ind. Microbiol. Biotechnol. 27 (5), 275.
Pfeiffer, T., Sanchez-Valdenebro, I., Nuno, J.C., Montero, F., Schuster, S., 1999. METATOOL: for studying metabolic networks. Bioinformatics 15 (3), 251–257.
Poolman, M.G., Venkatesh, K.V., Pidcock, M.K., Fell, D.A., 2004. A method for the determination of flux in elementary modes, and its application to *Lactobacillus rhamnosus*. Biotechnol. Bioeng. 88 (5), 601–612.
Ragauskas, A., Akinosho, H., Yee, K., Close, D., 2014. The emergence of *Clostridium thermocellum* as a high utility candidate for consolidated bioprocessing applications. Front. Chem., 2.
Riederer, A., Takasuka, T.E., Makino, S.-i, Stevenson, D.M., Bukhman, Y.V., Elsen, N.L., Fox, B.G., 2011. Global Gene Expression Patterns in *Clostridium thermocellum* as Determined by Microarray Analysis of Chemostat Cultures on Cellulose or Cellobiose. Appl. Environ. Microbiol. 77 (4), 1243–1253.
Roberts, S., Gowen, C., Brooks, J.P., Fong, S., 2010. Genome-scale metabolic analysis of *Clostridium thermocellum* for bioethanol production. BMC Syst. Biol. 4 (1), 31.
Rydzak, T., Grigoryan, M., Cunningham, Z., Krokhin, O., Ezzati, P., Cicek, N., Levin, D., Wilkins, J., Sparling, R., 2014. Insights into electron flux through manipulation of fermentation conditions and assessment of protein expression profiles in *Clostridium thermocellum*. Appl. Microbiol. Biotechnol., 1–14.
Rydzak, T., Levin, D., Cicek, N., Sparling, R., 2009. Growth phase-dependant enzyme profile of pyruvate catabolism and end-product formation in *Clostridium thermocellum* ATCC 27405. J Biotechnol. 140 (3–4), 169–175.
Rydzak, T., Levin, D.B., Cicek, N., Sparling, R., 2011. End-product induced metabolic shifts in *Clostridium thermocellum* ATCC 27405. Appl. Microbiol. Biotechnol. 92 (1), 199–209.
Rydzak, T., McQueen, P.D., Krokhin, O.V., Spicer, V., Ezzati, P., Dwivedi, R.C., Shamshurin, D., Levin, D.B., Wilkins, J.A., Sparling, R., 2012. Proteomic analysis of *Clostridium thermocellum* core metabolism: relative protein expression profiles and growth phase-dependent changes in protein expression. BMC Microbiol. 12, 214.
Sauer, U., Lasko, D.R., Fiaux, J., Hochuli, M., Glaser, R., Szyperski, T., Wüthrich, K., Bailey, J.E., 1999. Metabolic Flux Ratio Analysis of Genetic and Environmental Modulations of *Escherichia coli* Central Carbon Metabolism. J. Bacteriol. 181 (21), 6679–6688.
Shao, X., Raman, B., Zhu, M., Mielenz, J., Brown, S., Guss, A., Lynd, L., 2011. Mutant selection and phenotypic and genetic characterization of ethanol-tolerant strains of *Clostridium thermocellum*. Appl. Microbiol. Biotechnol. 92 (3), 641–652.
Stouthamer, A.H., 1973. A theoretical study on the amount of ATP required for synthesis of microbial cell material. Antonie van Leeuwenhoek 39 (1), 545–565.
Szyperski, T., Glaser, R.W., Hochuli, M., Fiaux, J., Sauer, U., Bailey, J.E., Wuthrich, K., 1999. Bioreaction Network Topology and Metabolic Flux Ratio Analysis by Biosynthetic Fractional ^{13}C Labeling and Two-Dimensional NMR Spectroscopy. Metab. Eng. 1 (3), 189–197.
Trinh, C.T., Unrean, P., Srienc, F., 2008. Minimal *Escherichia coli* cell for the most efficient production of ethanol from hexoses and pentoses. Appl. Environ. Microbiol. 74, 3634–3643.
Trinh, C.T., Wlaschin, A., Srienc, F., 2009. Elementary mode analysis: a useful metabolic pathway analysis tool for characterizing cellular metabolism. Appl. Microbiol. Biotechnol. 81 (5), 813–826.
Tripathi, S.A., Olson, D.G., Argyros, D.A., Miller, B.B., Barrett, T.F., Murphy, D.M., McCool, J.D., Warner, A.K., Rajgarhia, V.B., Lynd, L.R., Hogsett, D.A., Caiazza, N.C., 2010. Development of *pyrF*-Based Genetic System for Targeted Gene Deletion in *Clostridium thermocellum* and Creation of a pta Mutant. Appl. Environ. Microbiol. 76 (19), 6591–6599.
Tummala, S.B., Welker, N.E., Papoutsakis, E.T., 2003. Design of antisense RNA constructs for downregulation of the acetone formation pathway of *Clostridium acetobutylicum*. J. Bacteriol. 185 (6), 1923–1934.
Unkrig, V., Neugebauer, F.A., Knappe, J., 1989. The free radical of pyruvate formate-lyase. Eur. J. Biochem. 184 (3), 723–728.
van der Veen, D., Lo, J., Brown, S.D., Johnson, C.M., Tschaplinski, T.J., Martin, M., Engle, N.L., van den Berg, R.A., Argyros, A.D., Caiazza, N.C., Guss, A.M., Lynd, L.R., 2013. Characterization of *Clostridium thermocellum* strains with disrupted fermentation end-product pathways. J. Ind. Microbiol. Biotechnol. 40 (7), 725–734.
van Zyl, W.H., Lynd, L.R., den Haan, R., McBride, J.E., 2007. Consolidated bioprocessing for bioethanol production using *Saccharomyces cerevisiae*. Adv. Biochem. Eng./Biotechnol. 108, 205–235.
Wang, Y., Zhang, Z.-T., Seo, S.-O., Choi, K., Lu, T., Jin, Y.-S., Blaschek, H.P., 2015. Markerless chromosomal gene deletion in Clostridium beijerinckii using CRISPR/Cas9 system. J. Biotechnol. 200, 1–5.
Williams, T., Combs, J., Lynn, B., Strobel, H., 2007. Proteomic profile changes in membranes of ethanol-tolerant Clostridium thermocellum. Appl. Microbiol. Biotechnol. 74 (2), 422–432.
Yomano, L.P., York, S.W., Ingram, L.O., 1998. Isolation and characterization of ethanol-tolerant mutants of *Escherichia coli* KO11 for fuel ethanol production. J. Ind. Microbiol. Biotechnol. 20 (2), 132–138.
Zhang, Y., Lynd, L., 2003. Quantification of Cell and Cellulase Mass Concentrations during Anaerobic Cellulose Fermentation: Development of an Enzyme-Linked Immunosorbent Assay-Based Method with Application to *Clostridium thermocellum* Batch Cultures. Anal. Chem. 75 (2), 219–227.
Zhou, J., Olson, D.G., Argyros, D.A., Deng, Y., van Gulik, W.M., van Dijken, J.P., Lynd, L. R., 2013. Atypical Glycolysis in *Clostridium thermocellum*. Appl. Environ. Microbiol. 79 (9), 3000–3008.